The Moderate Size September 2019 M_w5.8 Silivri Earthquake Unveils the Complexity of the Main Marmara Fault Shear Zone

Hayrullah Karabulut[(1)], Sezim Ezgi Güvercin[(2)], Figen Eskiköy[(1)], Ali Özgun Konca[(1)], Semih Ergintav[(3)]

[1] Boğaziçi University, Kandilli Observatory and Earthquake Research Institute, Dept. of Geophysics, Istanbul, Turkey

[2] Yıldız Technical University, Faculty of Civil Engineering, Dept. of Geomatic Engineering, Istanbul, Turkey

[3] Boğaziçi University, Kandilli Observatory and Earthquake Research Institute, Dept. of Geodesy, Istanbul, Turkey

Corresponding author: Sezim Ezgi Güvercin (sezimguvercin@gmail.com).

Abstract

The unbroken section of the North Anatolian Fault beneath the Sea of Marmara is a major source of seismic hazard for the city of İstanbul. The northern and currently the most active branch, the Main Marmara Fault (MMF), is segmented within a shear zone and exhibits both partially creeping and locked behavior along its 150 km length. In September 2019, a seismic activity initiated near MMF, off-coast the town of Silivri, generating 14 earthquakes ≥ M_w3.5 in a week. The M_w5.8 Silivri earthquake, is the largest in the Marmara Sea since the 1963 M_w6.3 Çınarcık earthquake. Our analyses reveal that the activity started in a narrow zone (~100 m) and spread to ~7 km following an M_w4.7 foreshock within ~2 days. The distribution of relocated aftershocks and the focal mechanisms computed from regional waveforms reveal that the M_w5.8 earthquake did not occur on the MMF, but it ruptured ~60° north-dipping oblique strike-slip fault with significant thrust component located on the north of the MMF. Finite-fault slip model of the mainshock shows 8 km long rupture with directivity toward east, where the ruptured fault merges to the MMF. The narrow depth range of the slip distribution (10-13 km) and the aftershock zone imply that the causative fault is below the deep sedimentary cover of the Marmara Basin. The distribution of aftershocks of

the M_w5.8 event is consistent with Coulomb stress increase. The stress changes along MMF include zones of both stress decrease due to clamping and right-lateral slip, and stress increase due to loading.

Key words: Earthquake source observations; Seismicity and tectonics; Transform faults; Earthquake-source mechanism; Foreshocks; Aftershocks

Introduction

The North Anatolian Fault (NAF) is a major intracontinental transform fault which accommodates the Eurasia - Anatolia relative motion (Reilinger et al. 2006, Şengör et al. 2014). The slip rate along NAF is determined from GPS data as 20-27 mm/yr, increasing from east toward west (Reilinger et al. 2006). The NAF has produced large earthquakes as evidenced from historical records and instrumental period, including several M>7 earthquakes in 20th century, migrating from east to west (Barka et al. 2002, Figure 1a).

The only unbroken section of NAF since the beginning of the 20th century is along the Marmara Sea (Figure 1a). NAF splits into two main branches about 200 km east before the Sea of Marmara (Şengör, 1979), but most of the slip is accommodated along the northern branch (Le Pichon et al. 2001). Our study concerns this northern branch, the Main Marmara Fault (MMF), which comprises the submerged ~150 km long unruptured segment of the NAF within the Sea of Marmara. The MMF poses significant hazard for the large cities surrounding the region, particularly the megalopolis of Istanbul (Parsons et al. 2000, Figure 1b).

Observations from the microseismic activity show segmentation of the MMF corresponding to the four major basins of the Marmara Sea (Schmittbuhl et al. 2015). To the west, beneath the Tekirdağ basin (TB) and Central basin (CeB), MMF displays high seismicity rate distributed over a wide depth range (from surface to 17 km) (Figure 1). In the Kumburgaz basin (KB) located in the center of the Marmara Sea, seismicity is very sparse between a large zone from surface to 17 km. To the east, in the Çınarcık basin (ÇB), seismicity is uniformly distributed along the Princes Islands (PI) segment. It spreads within a narrow depth range between 8 and 14 km except at both ends of this basin where the seismicity extents vertically up to the surface.

Identification of the locked and creeping segments of the MMF has been the focus of several recent studies (Bohnhoff et al. 2013; Ergintav et al. 2014; Schmittbuhl et al. 2015). Schmittbuhl et al. (2015; 2016) presented microseismic activity and seismic repeaters as evidence of seismic creep in the CeB within a ~10 km zone (Figure 1b). The long term seismic repeaters clearly indicate seismic creep within ~10 km zone of CeB while the interpretation of the microseismic activity in terms of seismic creep for the entire CeB still needs to be confirmed. The acoustic measurements also yield a creep rate of ~11mm/year on the Western High, west of the CeB (Yamamoto et al. 2019). Along the KB segment, the modelling of the geodetic observations is interpreted as this segment can also be creeping (Ergintav et al. 2014), while the acoustic based sea bottom measurements in the eastern part of the KB show no sign of creep (Lange et al. 2019). From a seismological point of view, the absence of repeaters and low seismicity rate are interpreted as this segment is fully locked (Schmittbuhl et al. 2016).

In September 2019, the Marmara Sea region was struck with series of earthquakes including an M_w5.8 event. The September 26, 2019 earthquake (M_w5.8) occurred at the transition from the CeB segment to the KB segment (Figure 1b-c), where creep - locked transition needs to be better evaluated. Although the magnitude of the earthquake was not large, its location created concerns that it may trigger a larger earthquake along the MMF.

Whether this earthquake occurred along MMF, or on subsidiary faults remains unclear, specifically stress transfer related to this event on the MMF requires attention for a better characterization of seismic hazard in the region. In this study, we present high resolution seismicity, the geometry of the ruptured fault from focal mechanism solutions and evaluate the spatial and temporal evolution of the seismic activity. The results are used to compute finite fault slip distribution and Coulomb stress perturbations on the MMF.

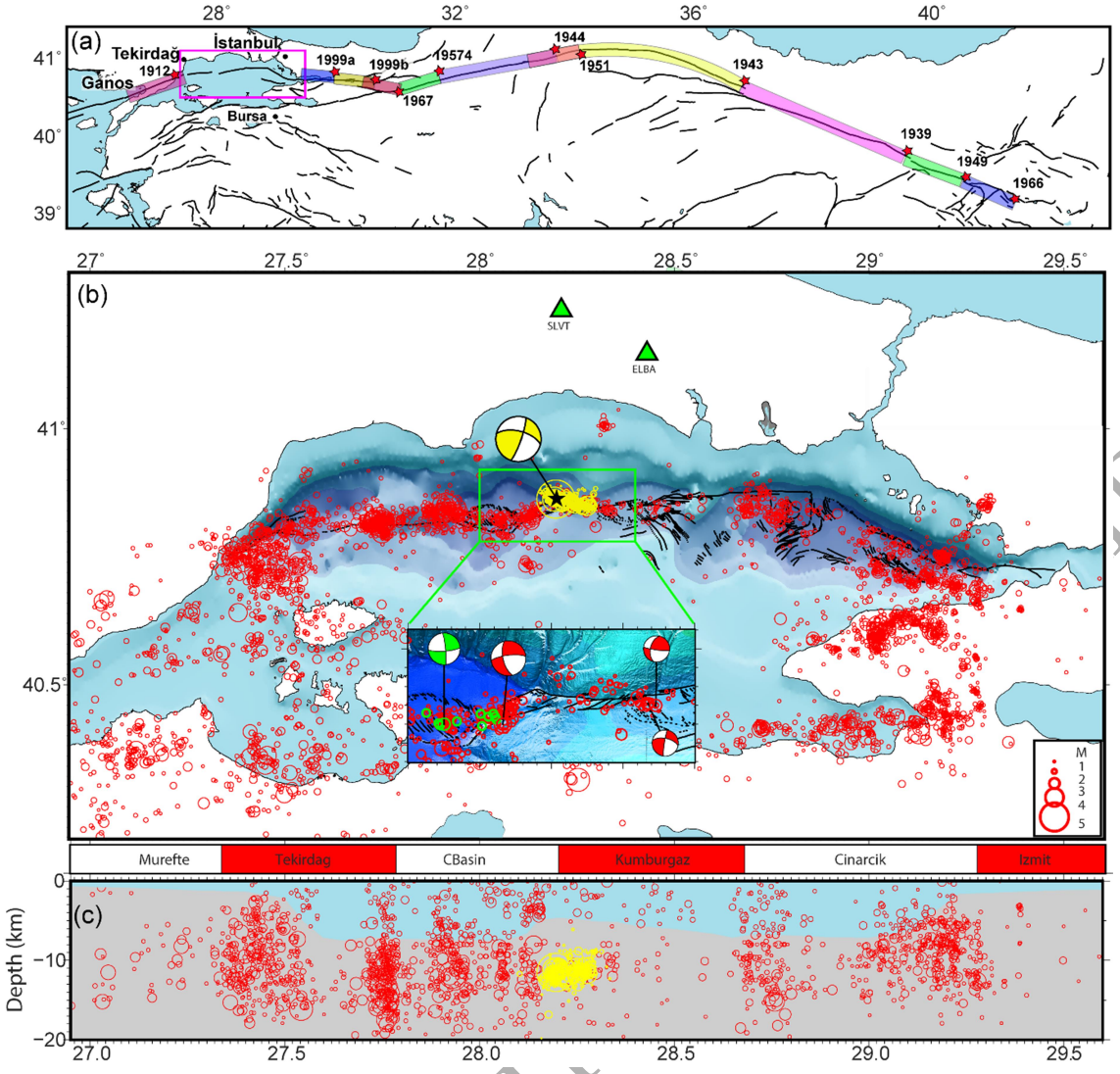

Figure 1. (a) The North Anatolian Fault and the major earthquakes (M_w>=6.9) along the fault since the December 26, 1939, Erzincan earthquake (Faults are from Emre et al. 2013, Rupture extents of large earthquakes are from Barka et al. 2002). (b) Map view of the seismicity in the Marmara Region during the period 2007–2015 (Schmittbuhl et al. 2015). In the Marmara Sea, four domains are introduced: the TB, the CeB, the KB, and the ÇB. Fault network is from Le Pichon et al. (2001). Focal mechanism of 2019 Silivri earthquake (yellow beach ball) with aftershock seismicity (yellow circles) is also shown. Inset figure shows the high resolution bathymetry and fault traces in the CeB (Le Pichon et al. 2001). Green circles in the inset figure show the locations of the seismic repeaters (Schmittbuhl et al. 2016). The red focal

mechanisms in the inset figure are determined from first motion polarities and the light green focal mechanism is the composite solution for the repeaters (Schmittbuhl et al. 2016). The green triangles show the location of the two seismic stations (SLVT, ELBA) used to detect earthquakes using template matching (c) Depth section showing the cross-section of the seismicity along the MMF within ±5km zone. 2019 sequence is shown by yellow circles. The blue region in the depth section shows the extent of low velocity basins along the MMF (See Bécel et al. 2010 for details).

Foreshock activity

The September 26, 2016, M_w5.8 Silivri earthquake was preceded by foreshocks which started 4 days earlier, with the largest, M_w4.7, on September 24. The activity had quite irregular behavior; 6 low magnitude events (M_l ~1.9-2.2) occurred on September 22. These 6 earthquakes were followed by ~36 hour quiescence which ended half an hour before the M_w4.7 earthquake. The aftershock activity of the M_w4.7 event continued until the M_w5.8 mainshock.

We provide a simple view of this foreshock-aftershock activity using the recordings of a broadband seismic station (SLVT), ~38 km north of the epicenter (Figure 2). Figure 2a shows the NS component velocity recording at the seismic station, SLVT, between September 21 and September 29. Instrument correction was applied to the trace and filtered between 2-10 Hz. The amplitudes of continuous trace were converted to approximate local magnitude assuming that the signals come from the epicenter of the mainshock.

The daily periodic variations in Figure 2a are related to the daytime anthropogenic activities. These high frequency-large amplitude variations hide low magnitude seismic events. Therefore, we cross-correlated the continuous seismic data with one of the foreshocks in order to uncover background seismic activity (Yang et al., 2009).

The high correlation coefficients observed in Figure 2b during September 22 show the initiation of the seismic activity at the epicentral region. The level of seismic activity was low between September 22 (15:00h) and September 24 (06:20h). Three foreshocks were detected between 06:20 and 08:00h (time of M_w4.7 event). The template event (M_l3.1) occurred ~30 min before M_w4.7 event and the latest foreshock ~0.5 sec earlier (Figure 2b and Inset). The cross correlation of the continuous data with the template detected more than 400 events (Figure 2b). The detection threshold for the cross correlation coefficient is selected as 0.5, which is above the background level. The activity following the M_w4.7 earthquake decayed in time following the Omori Law until the occurrence of M_w5.8 earthquake (Figure 2c). The extension of the observation period to September 15 did not show sign of any preceding seismic activity from the epicentral region. We also attempted to utilize other stations in the region for detection (Figure S1) but the SLVT station had the best signal quality and provided maximum number of events from template search.

The similarity of the waveforms detected during foreshock period is remarkable (Figure S2). The cross correlation coefficients among the waveforms are greater than 0.90 which indicates that they originate from the same zone with similar mechanisms. We also detected similar waveforms during the early aftershocks of the M_w4.7 event. Although the waveform of the M_w4.7 event has similarities to its foreshocks, it is contaminated by an event ~0.5 s earlier.

We selected 10 events (6 foreshocks and 4 aftershocks) to reveal their relative time-space distributions.

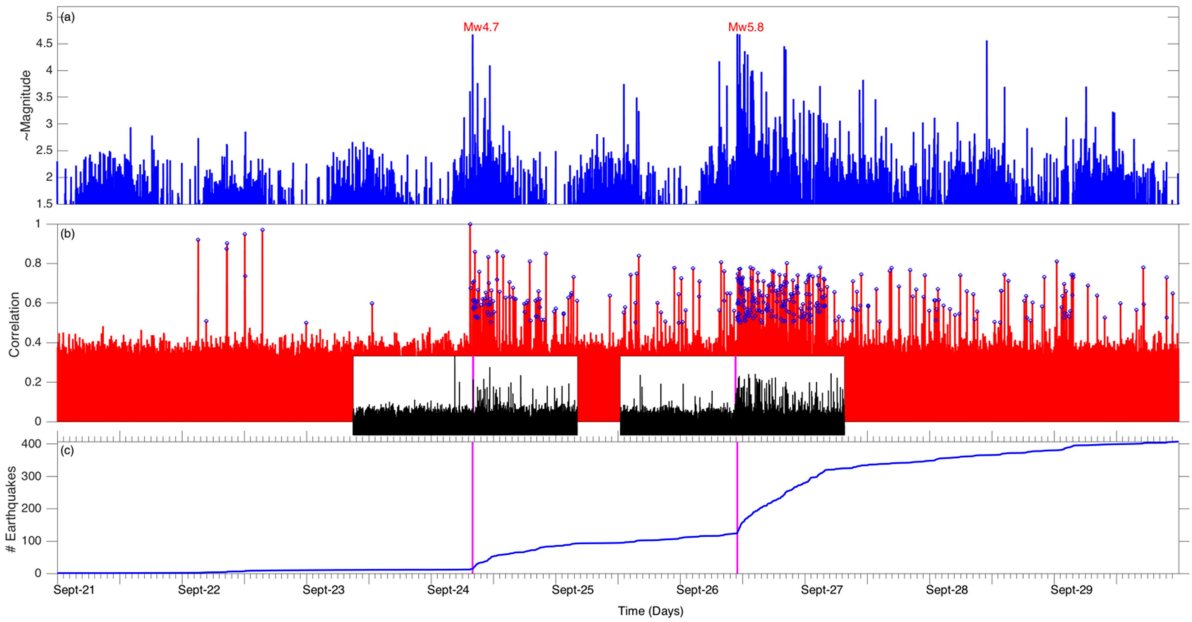

Figure 2. (a) NS component seismic recording at SLVT station between September 21 and September 29 (see Figure 1 for the station location). The data were clipped during M_w5.8 mainshock. The trace was filtered between 2-10 Hz with a Butterworth filter. The amplitudes of the whole trace are used to compute local magnitude. (b) Cross-correlation of the continuous recording with the foreshock (M_l3.1) preceding M_w4.7 event (cross correlation coefficient is one). Correlation coefficient of 0.5 was chosen as the event detection threshold. Blue circles indicate the detected events. Two inset figures (black traces) show ±3 hours close up windows of the correlation trace around the origin time of M_w4.8 (left) and M_w5.8 (right) events. (c) The normalized number of events detected by cross correlation. Pink vertical lines show the time of M_w4.7 and M_w5.8 earthquakes, respectively.

We used the time stretching of the waveforms to estimate the relative time shifts of each occurrence as more precise relative locations of the events were difficult due to the poor

station coverage (Figure S3-S4). This technique is used in coda wave interferometry to measure small changes in seismic wave velocities (Snieder et al. 2002). Here we use the same technique to compare the relative delay times of seismic coda for a pair of events (Bouchon et al. 2011). We computed the cross-correlation function of a pair of events using a 5 s moving window along both waveforms after aligning unfiltered waveforms on the *S* arrival. The first foreshock on September 22 was selected as the master waveform and cross-correlated with the other waveforms. The correlation coefficient stays high along the coda waves (during more than 10 s) (Figure 3a). The time shifts relative to the first events during high correlations are stable for each trace. The delays for the foreshocks (first 6 events) are small, i.e., less than one time sample which is 0.01 sec and increasing for the aftershocks, i.e. between 1-3 samples.

The small time delays of the S-coda of the foreshocks indicate that there are strong overlaps of the source areas during the foreshock period and very limited perturbations of the surrounding medium during the occurrences of each event. Using the formulation of Snieder and Vrijlandt (2005), which relates the relative positions of the sources δ, the average shear velocity $\beta \approx 3500$ m/s, and the variance of the time shifts, $\sigma_\tau = 0.01$, as $\delta^2 = 3\sigma_\tau \cdot \beta^2$, we obtain an estimate of the source position fluctuations as $\delta = 60m$. We computed the displacement spectra of the foreshocks using ~2.8 sec S-time window and estimated the corner frequencies using ω^2 source model (Schmittbuhl et al. 2016). The corner frequencies of the foreshocks are similar ~12.0 Hz, which corresponds to a source dimension of less than 100 m. The larger time shifts for the aftershocks show that they are several hundred meters away from the master event.

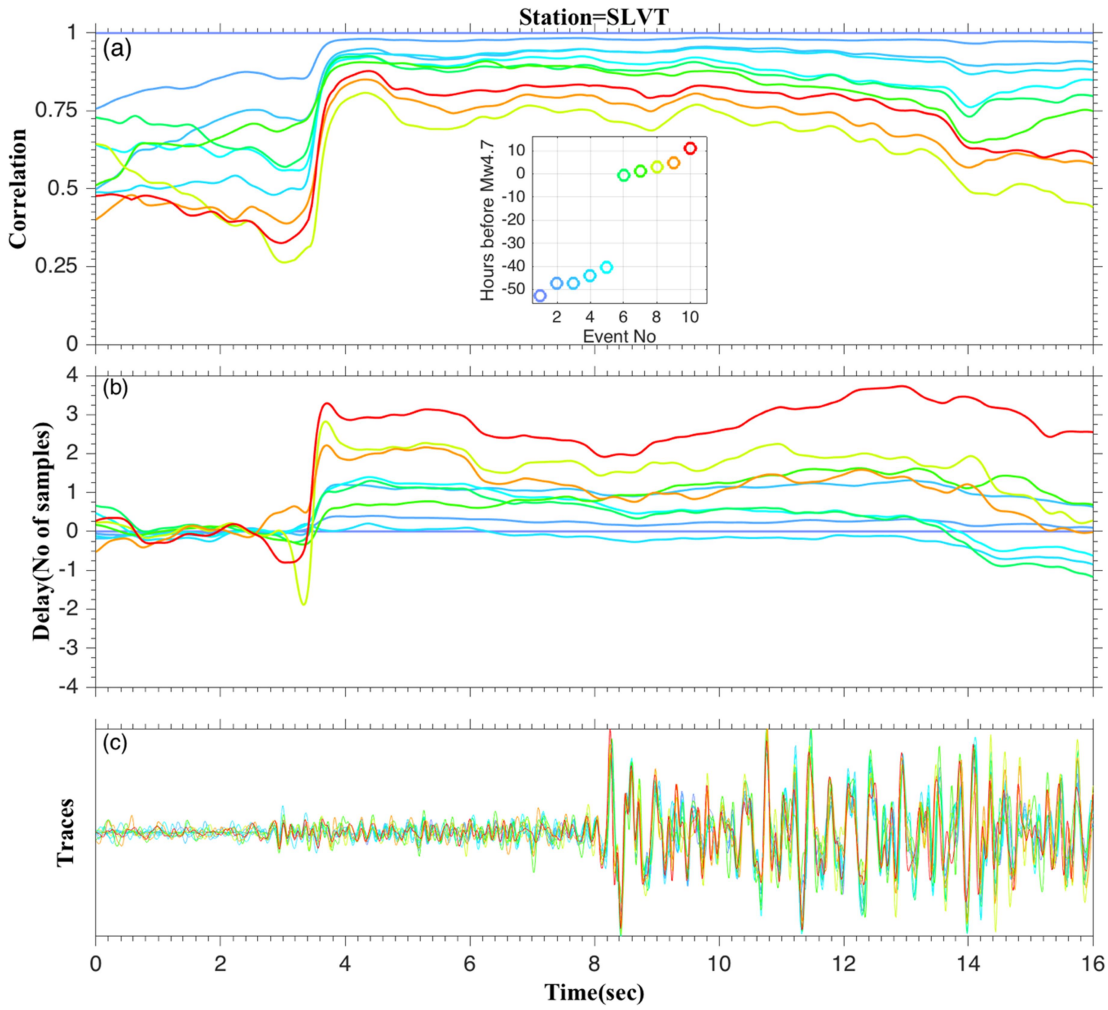

Figure 3. (a) Normalized cross-correlation coefficient of sliding window (5 sec) between the master event and all waveform (NS components) observed at SLVT (waveforms are shown in Figure. S2). The first event is selected as master event (lightest blue in all plots with correlation coefficient is one). Inset figure shows the time occurrences of the events relative to the M_w4.7 earthquake. (b) Time shifts between two waveforms for S wave and coda, in number of samples (0.01 sec). (c) Superimposition of the waveforms after normalization and alignment.

Mainshock and Aftershock Locations

We relocated the foreshocks and aftershocks between September 22 and September 28. We merged the catalogs of Disaster and Emergency Management Authority of Turkey (AFAD) (AFAD, 1990) and Boğaziçi University, Kandilli Observatory (KOERI) Regional Earthquake-Tsunami Monitoring Center (BDTIM) (KOERI, 2001). We compared the merged catalog with the detected events from cross-correlations in the previous step. After creating event database from the continuous waveforms of both agencies (KOERI and AFAD), we manually picked P and S phases and computed dentograms from the nearest stations to form waveform clusters. For each cluster a template event was selected and the phase readings were improved by cross-correlating the event waveforms in each cluster with the template event.

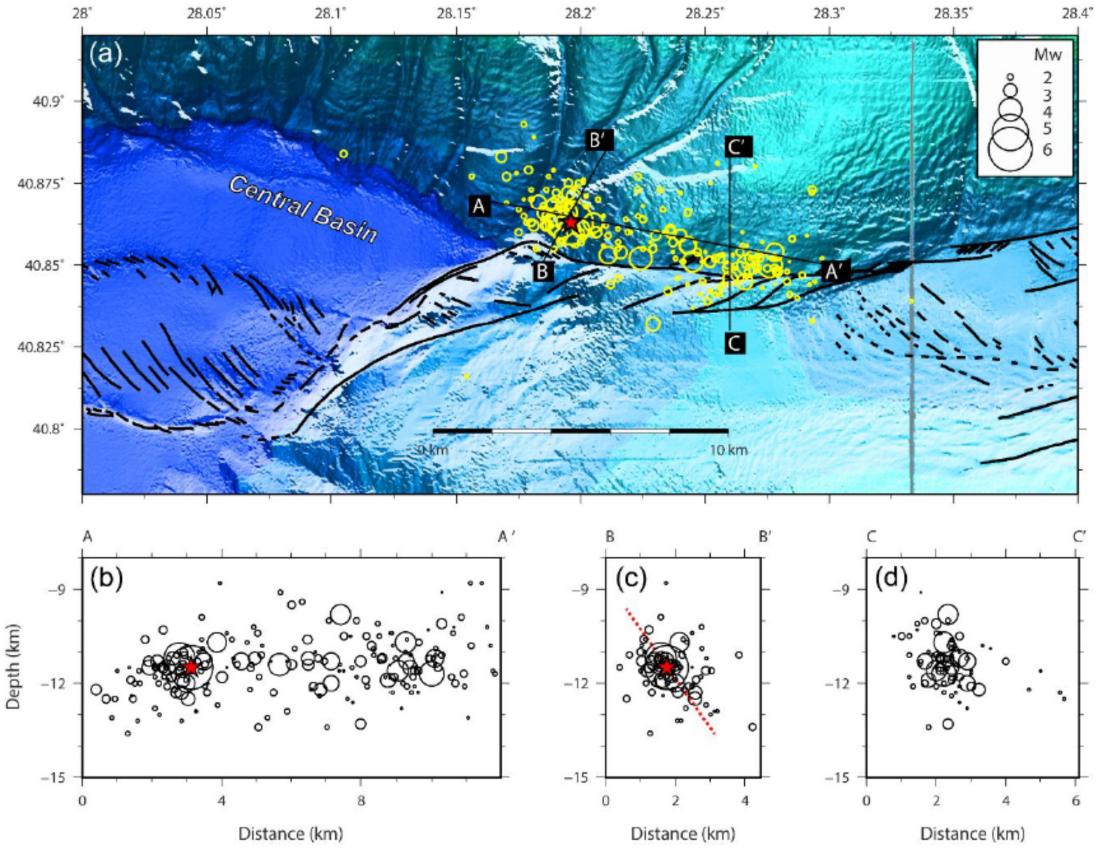

Figure 4. (a) Map view of the aftershock locations (yellow circles) during the first 8 days of seismic activity between September 22 and September 28. The magnitude scale is shown on top right. Black solid lines are the faults from Le Pichon et al. (2001). Red star shows the epicenter of the main shock. Cross sections along 3 profiles (b) AA' (c) BB' (d) CC' shown on the map view in (a). The red dashed line in BB' cross section shows a north dipping plane with 55°.

The final catalog contains 390 events between 22 September 2019 and 28 September 2019. We used HYPOCENTRE code (Lienert, 1986) for earthquake locations. A 1-D velocity model was computed using the VELEST inversion code (Kissling et al. 1994). The initial model from Karabulut et al. (2011) was used in the inversion and the deviations from 1-D velocity model are accounted in the station corrections. Average location uncertainties are

~0.9 and ~1.2 km for latitude and longitude, respectively. The mean of the depth uncertainty is ~1.5 km (The seismic station distribution and the uncertainties are provided in the Supplementary Materials, Figure S3-S4).

Figure 4a shows the aftershock distribution during the first 8 days of the activity from September 22. A total of 330 events were selected with horizontal uncertainties less than 2.0 km and vertical uncertainty less than 3.5 km. The total length of the activity zone is ~ 14 km with a strike of ~280 degree from north. The seismic activity is confined between 9 and 13 km depths and the hypocentral depths are slightly decreasing toward the east (Figure 4b). The vertical cross section of the westernmost extent of the activity shown in Figure 4c indicates that fault plane is dipping to north with ~55º. The cross section in the easternmost extent show no apparent dip (Figure 4d).

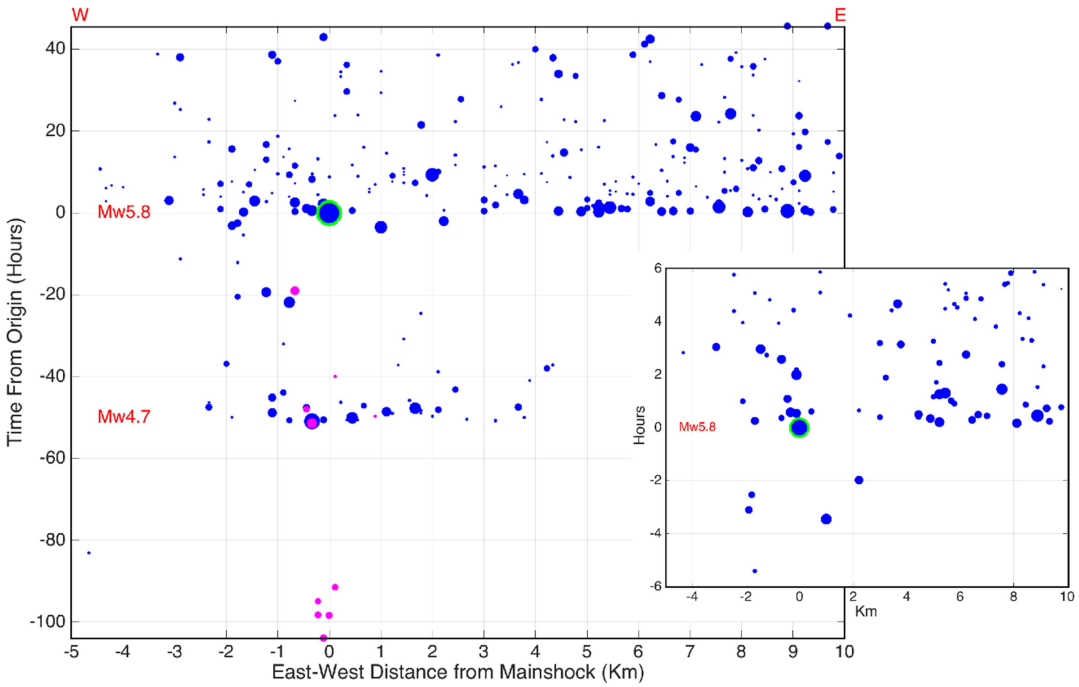

Figure 5: The evolution of the seismic activity between September 22 and September 28 along the ruptured fault plane in EW direction. The relative times and distances are computed

with respect to the mainshock origin time and its location (green circle). Inset figure shows the zoom ±6 hours from the mainshock origin time. The pink circles show the foreshocks and aftershocks with similar waveforms (Figure S2)

Figure 5 shows the temporal evolution of the seismic activity in EW direction. The relative distances are computed with respect to the longitude of the mainshock. The seismicity extends ~4 km to the west and ~10 km to the east. The aftershocks of the M_w4.7 earthquake extends to a zone of ~7 km in horizontal direction. This is roughly the rupture size of the M_w5.8 earthquake. The early aftershocks of M_w5.8 events (first 6 hours) are confined in a rectangular region with a length of ~8 km (large rectangular box in Figure S5) delineates well the ruptured fault plane. To the east, the activity further extents for ~5 km, confined within a zone of ~2 km width, much smaller than the western part (Figure 4).

Earthquake Source Mechanisms

The earthquake source mechanisms of M_w5.8, Silivri earthquake and its aftershocks were studied using 59 broad-band stations of KOERI- BDTIM and AFAD. Generalized Cut and Paste code by (Zhu and Helmberger 1996; Zhu and Ben-Zion 2013), which performs a grid search to obtain the strike, dip and rake angles as well as the moment magnitude by splitting and shifting the waveforms, was used to obtain the fault plane solutions (e.g. Tan et al. 2006, Wei et al. 2012, Zhu and Zhou, 2016). For the Green's functions, the frequency-wave number algorithm of Zhu and Rivera, 2002 was employed by using the 1D crustal velocity structure obtained in this study (Table S1, Supplementary material). Bootstrap analysis (Efron, 1979) was performed for the estimation of uncertainties of source mechanism parameters of the mainshock and the M_w4.7 foreshock, which shows that the strike, dip and

rake are resolved with ±10° uncertainty (See Supplementary material, Figure S6 for details). The waveform fits of three largest earthquakes are shown in Figures S7, S8, S9.

Table 1: Source mechanism solutions of the foreshocks, mainshock and aftershocks

Event No	Date-Time	Lat	Lon	Depth (km)	Centroid Depth (km)	Mag	Strike	Dip	Rake	VR%	Number of Stations
1	2019.09.24 07:30	40.86	28.19	11.6	-	3.0	286	59	171	68	11
2	2019.09.24 07:59	40.86	28.19	11.4	10.5	4.7	285	68	175	72	16
3	2019.09.26 07:32	40.86	28.21	10.7	10.0	3.6	292	66	170	60	16
4	2019.09.26 10:59	40.86	28.19	11.8	11.6	5.8	281	60	165	65	21
5	2019.09.26 11:26	40.85	28.28	11.7	11.4	4.1	77	74	152	51	18
6	2019.09.26 12:17	40.85	28.25	9.80	9.0	3.7	113	66	142	62	14
7	2019.09.26 12:26	40.85	28.26	11.6	11.6	3.7	76	80	137	61	14
8	2019.09.26 12:58	40.87	28.19	12.0	11.9	3.5	287	56	173	50	14
9	2019.09.26 20:02	40.85	28.28	11.3	11.9	3.5	80	72	136	58	13
10	2019.09.26 20:20	40.85	28.22	12.3	11.7	3.9	108	76	139	59	12
11	2019.09.28 11:03	40.85	28.27	10.7	10.0	3.8	89	78	137	56	17
12	2020.01.11 13:36	40.84	28.23	11.8	8.0	4.7	82	76	104	79	16

Source mechanisms of 12 earthquakes in the range of M_w3.0-M_w5.8, including the mainshock, are tabulated in Table 1. We fixed the latitude and longitude of the earthquakes from our revised catalogue. The station distribution for each event was selected carefully to avoid any bias which may result from the azimuthal coverage. A bandpass filter was applied to the waveforms between 10-25 s and 13-25 s, respectively for body and surface waves of the events with $M_w > 4$. For smaller events, band pass filters were applied between 7-25 s and 9-25 s, respectively for body and surface waves. In addition to the best-fitting mechanisms,

we performed depth grid searches to determine the centroid depths, except for the smallest event with M_w3.0. The calculated centroid depths are consistent with the relocated catalogue (Table 1, Figure S10). Figure 6 shows the focal mechanism solutions of three foreshocks with the largest M_w4.7, mainshock (M_w5.8) and 7 aftershocks with magnitudes between 3.0 and 4.1. The mechanisms are numbered based on their occurrence times. The overall appearance of the source mechanisms is consistent with the general trend and the kinematics of the MMF, east-west oriented right lateral strike-slip motion. The source mechanisms can be sorted into two groups.

In the western cluster (Figure 6, event numbers 1, 2, 3, 4, 8), where both the foreshocks and the mainshock are located, the earthquake mechanisms have a strike of ~280° from north, consistent with the orientation of the seismicity. The dips of these events are ~60° to the north with some reverse component (rake 150°±10°). In the eastern cluster (5, 6, 7, 9, 10, 11), the source mechanisms show E-W orientation (~270°) and steeply south dipping strike-slip faulting with larger reverse components. The event 12 (Figure 6, green beachball) occurred more than 2 month later and has almost pure reverse mechanism. The strike of this event is consistent with the strike of the second group events in the east.

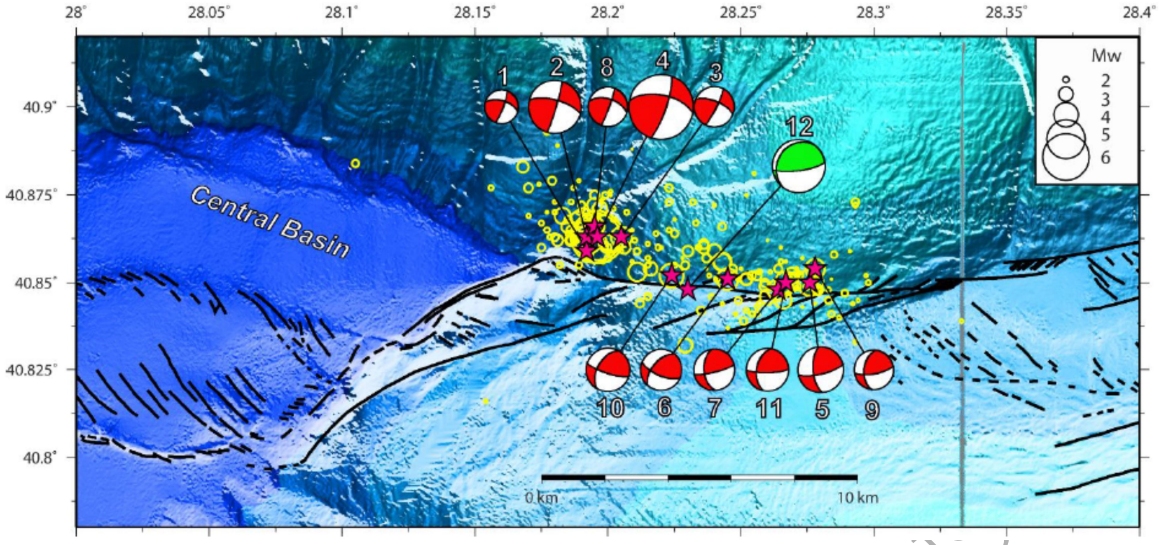

Figure 6: Map view of aftershock distribution and focal mechanisms. Yellow circles show the epicenters of aftershock activity of the first 8 days (M>1). The green beachball is the focal mechanism of the M_w4.7 earthquake which occurred on January 11, 2020, 75 days after the mainshock. Pink stars the epicenters of the earthquakes with the focal mechanism solutions listed in Table 1. Solid black lines indicate active faults from Le Pichon et al. (2001). The focal mechanisms are numbered by their occurrences in time.

The last event (January 11, 2020 M_w4.7) is located near the end of the ruptured fault between two fault planes with two different dip angles (Figure 6). The absence of strike-slip component suggest that this event might be at the eastern termination of the fault associated with the western cluster including the mainshock.

Finite-Fault Model

In order to find the slip distribution, we performed an inversion of strong motion data using the finite-fault inversion of Ji et al. (2002), which searches for the best-fitting solution for the slip on a planar fault and kinematic parameters of the earthquake by minimizing the error using a simulated annealing algorithm.

We built a fault plane based on the point source solution of the mainshock (strike/dip of 281°/60°, Table 1). We chose the right-lateral fault plane as it is consistent with the aftershock distribution as well as the general right-lateral behavior of the NAF system (Figure 6). Rake is allowed to vary between 130° and 180°, rupture velocity between 1.7 and 3.7 km/s and rise time between 0.4 and 1.2 s. The fault plane is constructed using 25 sub-faults along strike and 11 along dip, where each sub-fault has a size of 0.8 km $\times$ 0.5 km, respectively. Green's functions are calculated using the frequency wavenumber algorithm of Zhu and Rivera, 2002 and using the velocity model obtained in this study (Table S1).

The moderate size of the earthquake and lack of geodetic data due to submarine epicenter of the earthquake makes it challenging to obtain a reliable solution. Based on our initial attempts using point sources, we only used 7 strong-motion stations from AFAD and one station (BOTS) from KOERI's Istanbul Early Warning and Rapid Response station for the finite-fault analysis. The acceleration records are filtered between 1 s to 30 s and integrated twice to obtain displacement waveforms.

As an initial step, we predicted the displacement waveforms for a point source with a symmetric triangular source-time function of 4 s duration (Figure S11). The complexity of the radial and vertical component waveforms, which are possibly related to complex P-S conversions, enforced us to use only the transverse components that recorded the source process quite well. The point source calculations show some directivity; the SH waves with 4 s symmetric source function fit the stations on the west of the epicenter (Figure S11b), while the recorded displacements are shorter in the east with sharper S wave onsets (Figure S11a).

Based on the point source calculations, the data and synthetics are aligned on their S wave arrivals. Initially, we attempted a finite-fault model where we allowed only up-dip rupture (fault plane between 7.5 and 11.5 km depths). The resulting slip distribution concentrates at the deeper end of the fault plane (Figure S12). Therefore we decided to use a fault plane based on the seismicity distribution, between 9.5 km and 13.5 km allowing both up-dip and down-dip slip. Allowing down-dip slip increases variance reduction to 66.9%, while the initial up-dip fault plane inversion has only 62.8% variance reduction. The comparison of two slip distributions and their fits to the strong-motion waveforms are shown in Figure S12. Although the slip distributions are quite similar, with similar lateral directivities and narrow depth intervals, the improvement in variance reduction, favors the down-dip slip model as the final slip model.

In order to ensure that the east directivity and narrow depth confinement around the hypocenter is a robust feature of our finite-fault model, we performed an additional test by manually generating a bilateral slip distribution that propagates up-dip to 7 km depth (Figure S13a). The predicted SH waveforms (Figure S13b) shows that significant up-dip propagation over-predicts the amplitudes of waveforms at some stations. In addition, the bilateral rupture does not fit the sharp waveforms observed to the east of the rupture. Thus, we conclude that

the M_w5.8 earthquake ruptured a very narrow along-dip zone below the depth of 10 km and the dominant rupture propagation toward east.

The resulting finite-fault slip distribution shows ~8 km long bilateral rupture between the depths of 11 and 13 km (Figure 7). The slip values are higher toward the east reaching to the maximum value of 100 cm. The rupture zone is longer in the east (5 km) compared to the west (3 km). The average rupture velocity is around 2 km/s but slightly faster toward east, as can be inferred from the relative sharpness of the SH wave pulses in Figure S14. The majority of the seismic activity is located in the low slip areas. It appears that the seismicity in the eastern end of the high slip region extends further than the slip area; while to the west, the seismicity is confined to the slip zone (Figure 7).

In order to test the effect of hypocentral depth uncertainty on the slip model, we modelled the finite-fault slip by shifting the hypocenter 1 km up and down, which is in the order of the calculated uncertainty of the hypocenter depth (±1.2 km). As clear from the resulting finite-fault models (Figure S15), shifting the hypocenter depth 1 km up or down does not change the slip distribution around the hypocenter. Therefore, we conclude that the slip distribution can be shifted up or down within the error margin of the hypocenter depth. Considering that stations are about 50-100 km away from the source and there is no near-source geodetic data, this result is expected.

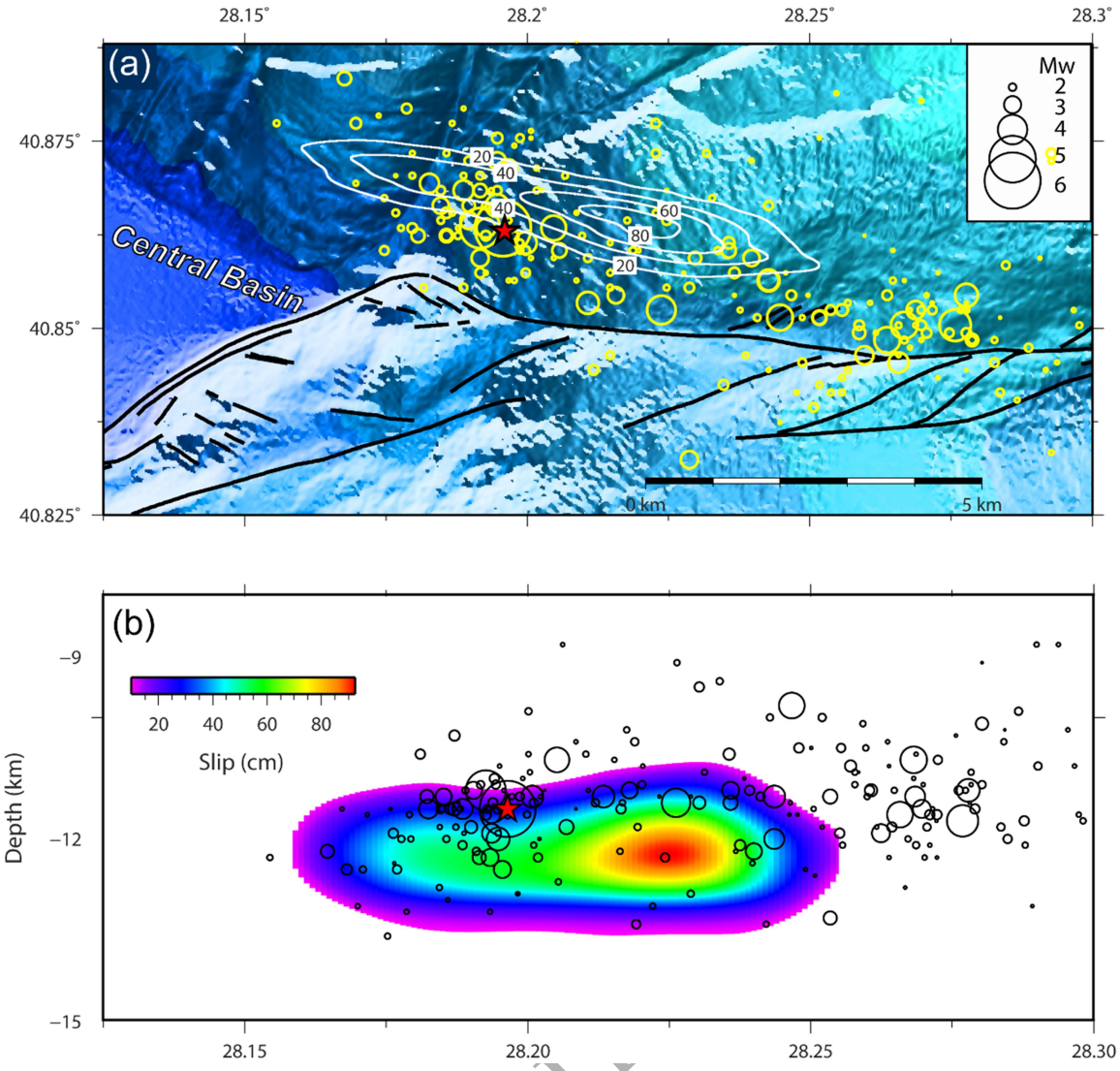

Figure 7. (a) Map view of slip distribution for the best fitting north-dipping fault with seismicity projected on the rupture plane. Faults are from Le Pichon et al. (2001). (b) Fault plane view of the slip distribution. Red star shows the hypocenter of the mainshock.

Coulomb Stress Changes

We investigated the correlation between Coulomb stress changes due to the mainshock and its aftershocks distribution. Coulomb stress changes due to M_w5.8 event were computed on the optimally oriented strike-slip faults (Toda et al. 2011) using the regional stress values for the Central Marmara basin by Örgülü (2011) (with principal stress directions (azimuth/plunge) of σ_1=131 °/12 °,σ_2=-90 °/75 °,σ_3=39 °/10 °).

We calculated Coulomb stress changes for 3 different values of friction coefficients (μ =0.3, 0.4 and 0.5) at 12 km depth (Figure S16). As the Coulomb stress changes do not significantly vary for 3 different friction coefficients and considering the ruptured fault has a strike-slip character with previously unknown seismic activity we used μ = 0.4 for our final computation. We did not test μ > 0.5 and μ < 0.3, as they are more representative for very soft and dry faults (Beeler et al. 1996). The Coulomb stress changes are displayed at 10 km and 12 km depths with the mainshock and aftershock seismicity for 9–11 km and 11–13 km depth ranges, respectively (Figure 8). Stress increase is observed up to ~2 bars near the terminations of the rupture plane. The aftershock activity correlates well with the calculated coulomb stress changes (Figure 8b).

Due to uncertainty of the hypocenter depth, we also estimated the Coulomb stress changes on optimally oriented faults using the finite-fault models (Figure S15) with hypocenter depths of 10 and 12 km. The comparison of the Coulomb stress changes with the aftershock locations (Figure S17) shows that the aftershock distribution is consistent with a deeper hypocenter. For the shallower hypocenter, significant number of aftershocks are located in the stress decrease zones, especially those located between 11 and 13 km. Thus, we conclude that a

shallower (< 11 km) hypocenter depth and related slip distribution are inconsistent with the aftershock locations which supports a deep slip zone for the mainshock.

We also tested whether the September 2019 earthquake caused stress increase on the MMF using the fault geometry from Le Pichon et al. (2001). The results show that the MMF experiences stress increase at depths between 7 and 10 km, to the south and east of the ruptured fault (Figure S18).

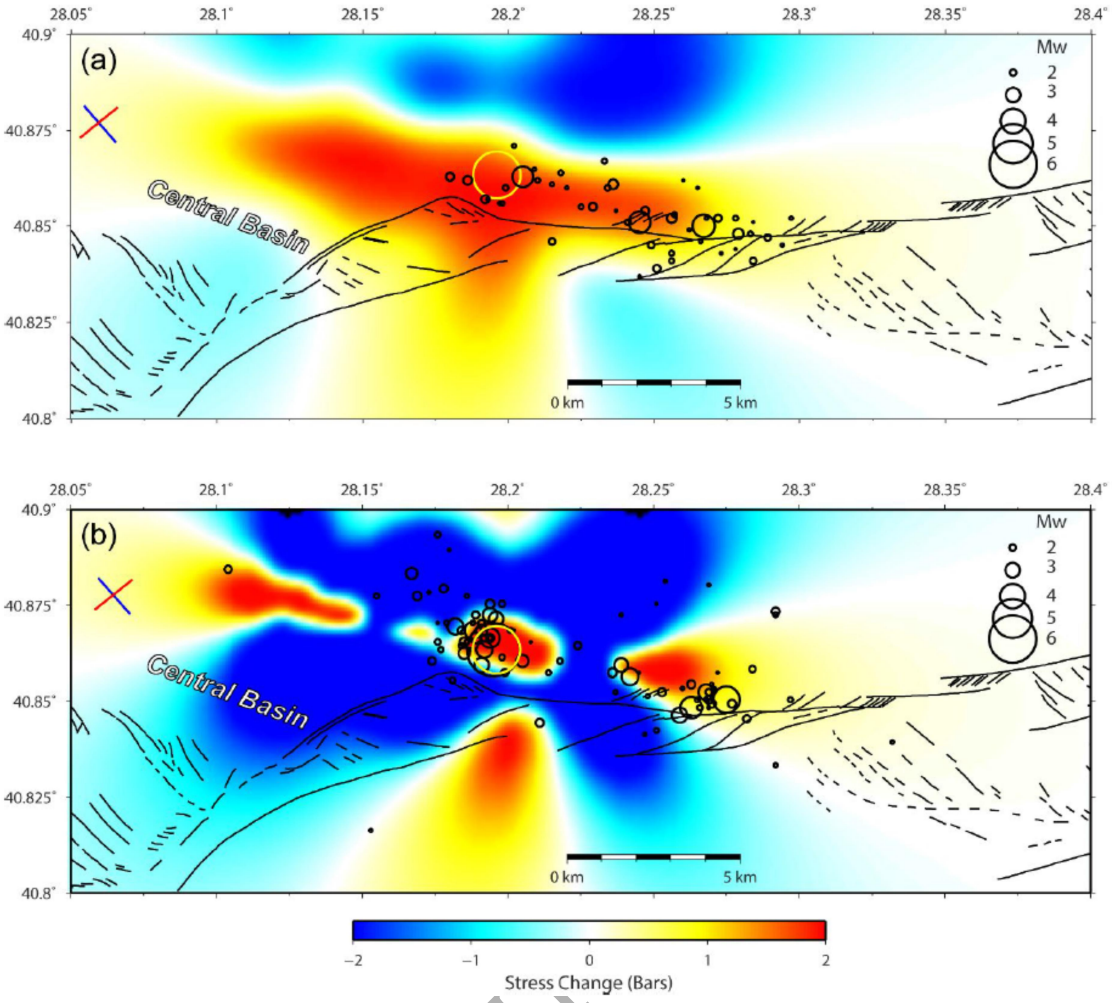

Figure 8. The coulomb stress changes, on optimally oriented faults for the slip model obtained in this study. The black circles show the aftershocks (M ≥ 1) during the first 3 days following the mainshock. Yellow circle represents the epicenter of the mainshock. Faults are from Le Pichon et al. (2001). a) The Coulomb stress changes displayed at 10 km. Seismicity is between 9 and 11 km. b) The Coulomb stress changes displayed at 12 km depth. Seismicity is between 11 and 13 km.

Discussion

The 2019 Silivri earthquake activity stimulates discussions on seismic interactions, nucleation, fault structure and seismic hazard in a seismic gap expected to be filled in near future in the Marmara Sea.

Spatiotemporal Evolution of the Earthquake Sequence

The foreshocks of the recent large earthquakes have been on the focus of the alternative physical processes of the earthquake nucleation. The seismic activity preceding the M_w5.8 2019 Silivri earthquake provides a distinct observational view for the earthquake rupture process.

The foreshock activity of 2019 Silivri earthquake started with small magnitude events (1.9-2.2), followed by a quiescence period of ~24 hours which is followed by an M_w4.7 earthquake. Small relative time delays of S waves and coda (less than 0.01sec) imply that the activity preceding the M_w4.7 including the M_w4.7 event took place in a zone of less than 100 m with overlapping patches of ~50 m. The perturbation due to M_w4.7 earthquake spread the activity over a zone of ~7 km in EW direction in the following two days. The M_w5.8 mainshock occurred two days later following the Omori decay of the M_w4.7 aftershocks. Comparison of the aftershocks of the M_w4.7 with the slip distribution of the M_w5.8 mainshock shows that the mainshock ruptured almost the same area of the foreshock activity. Interestingly, the M_w4.7 January 11, 2020 earthquake that occurred along the same fault segment generated very little number of aftershocks.

We suggest two possible explanations for this phenomenon. First possible explanation is that the ruptured fault was in a critical state with some heterogeneous distribution of high stress region. Hence, the stress perturbation of the M_w4.7 earthquake was sufficient to spread the activity to the whole fault segment. Eventually one of these earthquakes triggered the mainshock and ruptured the entire segment (Ellsworth & Beroza, 1995). The later January, 2020 M_w4.7 aftershock occurred on a patch that had not ruptured in the September 2019 sequence. But since the fault had released most of its stress before, it did not generate the large number of aftershocks as the September 2019 M_w4.7 foreshock.

Second explanation is that the process was governed by slow slip. The ~100 m zone of initial activity might be the nucleation point of the slow slip event. As the slow slip propagated it eventually triggered the M_w5.8 mainshock. The recent studies of foreshocks of several large earthquakes suggest a physical process of continuous slow deformation prior to nucleation (Kato et al., 2012; Kato et al. 2016; Bouchon et al., 2011; Bouchon et al., 2013). However, in the absence of near-field observations, it is difficult to differentiate whether the activity is governed by slow-slip or triggering of earthquakes in a heterogeneous stress distribution environment.

The Faulting Related to the Activity and Its Relation to the MMF

The fault plane solutions of M_w4.7 foreshock and M_w5.8 mainshock are similar (Table 1). Both are dipping toward north (~60°) with reverse component (rake 160°±10°) and have a strike of ~280°. The almost E-W orientation of the aftershock distribution is consistent with the strike of the mainshock fault plane solution with right-lateral slip (Figure 6). The

aftershock activity forms a subparallel geometry to the MMF identified on the high resolution bathymetry and seismic reflection images (Şengör et al. 2014).

Seismicity and high resolution seismic images in the central part of the Marmara Sea show that the present route of the active MMF follows the southern margin of the PDZ (Le Pichon et al. 2001; Şengör et al. 2014). The available source mechanism solutions of the earthquakes on the southern part of the shear zone show dominant strike slip motions with normal components (Inset of Figure 1) unlike the 2019 activity. Several findings from this study reveal the nature of faulting related to the September 2019 sequence. First of all, the relatively shallow dip angle of the ruptured fault (~60°) is inconsistent with the dip of the MMF, which is 80°–90° (Şengör et al. 2014). The seismicity distribution and the strike of the source mechanisms (280°–285°) suggest a fault orientation subparallel to the MMF with a strike of ~265° around the activity zone. Lack of aftershocks to the west of the mainshock shows that the fault does not extend further toward the west. Furthermore, the aftershocks at the eastern end of the activity zone show changes in fault strike and dip which is more consistent with MMF (Figure 4). In addition, the depth confinement of the activity (9-13 km) shows no penetration into shallower depths which are covered with thick sediments down to a depth of ~6 km.

Based on these observations, we suggest that this earthquake sequence, including the mainshock, ruptured a secondary fault beneath the sedimentary layers in the shear zone on the north of the MMF. Considering its orientation and proximity to the MMF, it can be inferred that the ruptured fault connects to the PDZ on the KB segment (Figure 1), where the deformation is more localized with a continuous and linear geometry toward the Princes

Islands. There is no evidence that the causative fault structure has any continuity up-dip or toward the west.

While the activity on the west, including the mainshock are all consistent with north dipping fault plane, activity on the east shows a steep south-dipping fault plane with more significant thrust component. Based on the geometry and source mechanisms of the aftershocks (Figure 6 and Table 1 event numbers 5,6,7,9,10,11), we infer that this activity to the east is located in the PDZ of the MMF and dipping to south, opposite to the mainshock.

Thrust component of the Earthquakes

One remarkable feature of this seismic activity was the significant thrust component observed on all the source mechanism solutions. A possible explanation for the thrust component is the heterogeneity of the interseismic behavior along the MMF which might have led to a local compression in the epicentral region of the 2019 Silivri activity. To the west of this activity, there is evidence of partial creep of the fault from seismicity, repeating earthquakes and geodesy along the CeB and western high (Ergintav et al. 2014; Schmittbuhl et al. 2016; Yamamoto et al. 2019). On the other hand, a recent submarine geodetic study to the east of the epicentral area on the center of the Central High (within a 500m zone) has observed no evidence of creep (Lange et al. 2019). If the zone of the 2019 earthquake lies between a partially creeping zone to the west (CeB) and a partially locked zone to the east (KB), for a right-lateral system, it can be expected for the given fault orientation to have compression on a fault with a WNW strike.

It is also possible that the thrust component observed in all source mechanisms might be related to the changes of the shear zone width and local stress orientations. Although the strike-slip motion along CeB is predominantly accommodated by the faults along the southern margin, there is still a wider deformation zone (~10 km). Further east along central high, the PDZ is localized to a much narrower zone. This transition might cause a local rotation of the regional stress tensor leading to an oblique shortening (Merzer and Freund 1975).

The importance of the off-fault seismicity along the whole NAF before the initiation of the M_w>7 earthquakes since 1939 is pointed out by Dewey (1976). Most of the off-fault seismic activity before the large earthquakes along NAF since 1939 was extensional in nature, reducing the normal stress and possibly facilitating the initiation of large earthquakes. The pre-earthquake activity along the NAF during 1939 and migration mostly occurred on the south of the NAF. In contrast, the 2019 Silivri earthquake occurred on the north of PDZ of the MMF and has a thrust component. On one hand 2019, M_w5.8 earthquake led to Coulomb stress increase on the shallower depths along the MMF (Figure 8, Figure S18). But at the same time, it released some of the shear stress along the fault zone and the thrust component led to clamping of the main fault due to increase in normal stress. As a result, although it promoted aftershocks at the eastern termination and up-dip of the rupture, the influence on the MMF was not significant.

Conclusion

2019 Silivri earthquake ruptured a fault segment within the shear zone of the MMF, east of the CeB. The deformation leading to the M_w5.8 mainshock started from a localized zone and spread over a wider zone within 2 days as a result of a M_w4.7 event. The finite-fault analysis shows that the rupture propagated bilaterally, down-dip and broke 8 km long fault segment at depths between 10 and 13 km. The spatial distribution of aftershocks, the geometry of the ruptured fault, and the variations on the source mechanisms suggest that the earthquake ruptured a relatively inactive structure in the shear zone north of the MMF. The earthquake led to a stress increase along a 10 km length of the MMF between CeB and KB segments while decreasing the stress further west along southwest of the CeB. These relatively old-hidden structures which are not observed on the seismicity and seismic images pose additional dangers for seismic hazard in the region.

Acknowledgement

We would like to thank editor Sidao Ni, Michel Bouchon and two anonymous reviewers for their particularly detailed comments which improved the quality of the manuscript.

References

AFAD (Disaster and Emergency Management Presidency) (1990): National Seismic Network of Turkey (DDA). International Federation of Digital Seismograph Networks. http://tdvm.afad.gov.tr/

Barka, A., 1997. Neotectonics of the Marmara region in active tectonics of northwest Anatolia. In: Schindler, C., Pfister, M. (Eds.), The Marmara Poly-Project, Hochschulverlag AG an der ETH, Zurih, pp. 55–87.

Bécel, A., Laigle, M., de Voogd, B., Hirn, A., Taymaz, T., Yolsal-Cevikbilen, S., & Shimamura, H. (2010). North Marmara Trough architecture of basin infill, basement and faults, from PSDM reflection and OBS refraction seismics. *Tectonophysics*, *490*(1–2), 1–14. https://doi.org/10.1016/j.tecto.2010.04.004

Beeler, N.M., Tullis, T.E., Blanpied, M. L. & Weeks, J.D. (1996). Frictional behavior of large displacement experimental faults. Journal of Geophysical Research,101(4)8697-8715.https://doi.org/10.1029/96JB0041

Bohnhoff, M., Bulut, F., Dresen, G., Malin, P. E., Eken, T., & Aktar, M. (2013). An earthquake gap south of Istanbul. *Nature Communications*, *4*(November 2015). https://doi.org/10.1038/ncomms2999

Bouchon, M., Karabulut, H., Aktar, M., Özalaybey, S., Schmittbuhl, J., & Bouin, M. P. (2011). Extended nucleation of the 1999 M_w 7.6 Izmit earthquake. *Science*,

331(6019),

877–880. https://doi.org/10.1126/science.1197341

Bouchon, M., Durand, V., Marsan, D., Karabulut, H., & Schmittbuhl, J. (2013). The long precursory phase of most large interplate earthquakes. Nature Geoscience, 6(4), 299–302. doi:10.1038/ngeo1770

Dewey, J. W. (1976). Seismicity of Northern Anatolia. *Bulletin of Seismological Society of America*, *66*.3, 843–868

Efron, B. (1979). Bootstrap Methods: Another Look at the Jackknife. *The Annals of Statistics.* 7.1,1-26

Ellsworth, W. L. and Beroza, G. C. (1995). Seismic Evidence for an Earthquake Nucleation Phase. *Science.* 268, 851–855.

Emre, Ö., Duman, T. Y., Özalp, S., Şaroğlu, F., Olgun, Ş., Elmacı, H., & Can, T. (2018). Active fault database of Turkey. *Bulletin of Earthquake Engineering*, 16(8), 3229-3275.

Ergintav, S., Reilinger, R. E., Çakmak, R., Floyd, M., Cakir, Z., Doğan, U., King R. W., McClusky,S., Özener, H., (2014). Istanbul's earthquake hot spots: Geodetic constraints

on strain accumulation along faults in the Marmara seismic gap. *Geophysical*

Research

Letters, 41, 5783–5788, https://doi.org/10.1002/2014GL060985

Ji, C., Wald, D. J. and Helmberger, D. V., 20027. Source description of the 1999 Hector Mine, California, earthquake, part I: wavelet domain inversion theory and resolution analysis, *Bull. Seismol. Soc. Am.* **92** (4), 1192–1207.

Karabulut, H., Schmittbuhl, J., Özalaybey, S., Lengliné, O., Kömeç-Mutlu, A., Durand, V., Bouin, M. P. (2011). Evolution of the seismicity in the eastern Marmara Sea a decade before and after the 17 August 1999 Izmit earthquake. *Tectonophysics*, *510* (1–2), 17–27. https://doi.org/10.1016/j.tecto.2011.07.009

Kato, A., Obara, K., Igarashi, T., Tsuruoka, H., Nakagawa, S. & Hirata, N. (2012). Propagation of slow slip leading up to the 2011 M_w 9.0 Tohoku-Oki earthquake. *Science* 335, 705708

Kato, A., Fukuda, J., Kumazawa, T., & Nakagawa, S. (2016). Accelerated nucleation of the 2014 Iquique, Chile M_w8.2 earthquake. *Sci. Rep.* 6, 24792.

Kissling, E., Ellsworth, W. L., Eberhart-Phillips, D., & Kradolfer, U. (1994). Initial reference models in local earthquake tomography. *Journal of Geophysical Research*, *99*(B10). https://doi.org/10.1029/93jb03138

KOERI (Kandilli Observatory and Earthquake Research Institute), Bosphorus Univ. (2001): Bogazici University Kandilli Observatory And Earthquake Research Institute.

International Federation of Digital Seismograph Networks. Dataset/Seismic Network. 10.7914/SN/KO. https://doi.org/10.7914/SN/KO

Laigle, M., Bécel, A., de Voogd, B., Hirn, A., Taymaz, T., & Ozalaybey, S. (2008). A first deep seismic survey in the Sea of Marmara: Deep basins and whole crust architecture and evolution. *Earth and Planetary Science Letters*, *270*(3–4), 168–179. https://doi.org/10.1016/j.epsl.2008.02.031

Lange, D., Kopp, H., Royer, J. Y., Henry, P., Çakir, Z., Petersen, F., Géli, L. (2019). Interseismic strain build-up on the submarine North Anatolian Fault offshore Istanbul. *Nature Communications*, *10*(1). https://doi.org/10.1038/s41467-019-11016-z

Le Pichon, X., Lepinay, B. M. De, Meyer, B., Armijo, R., Go, N., Saatc, R., & Tok, B. (2001). The active Main Marmara Fault. *Earth and Planetary Science Letters*, *192*.

Le Pichon, X., Chamot-Rooke, N., Rangin, C., & Sengör, A. M. C. (2003). The North Anatolian fault in the Sea of Marmara. *Journal of Geophysical Research: Solid Earth*, *108*(B4), 1–20. https://doi.org/10.1029/2002jb001862

Le Pichon, X., & Kreemer, C. (2010). The Miocene-to-Present Kinematic Evolution of the Eastern Mediterranean and Middle East and Its Implications for Dynamics. *Annual Review of Earth and Planetary Sciences*, *38*(1), 323–351. https://doi.org/10.1146/annurev-earth-040809-152419

Lienert, B. (1986). HYPOCENTER: An earthquake location method using centered, scaled, and adaptively damped least squares. *Bulletin of the Seismological Society of America*,
76(3), 771–783.

Merzer, A. M., & Freund, R. (1975). Buckling of Strike-Slip Faults-in a Model and in Nature. *Geophysical Journal of the Royal Astronomical Society*, *43*(2), 517–530. https://doi.org/10.1111/j.1365-246X.1975.tb00645.x

Örgülü, G. (2011). Seismicity and source parameters for small-scale earthquakes along the splays of the North Anatolian Fault (NAF) in the Marmara Sea. *Geophysical Journal International*, *184*(1), 385–404. https://doi.org/10.1111/j.1365-246X.2010.04844.x

Parsons T., Toda S., Stein, R.S., Barka A., Dieterich J.H. (2000). Heightened odds of large earthquakes near İstanbul: An interaction-based probability calculation. Science. 288(5466):661-5. DOI: 10.1126/science.288.5466.661

Reilinger, R., McClusky, S., Vernant, P., Lawrence, S., Ergintav, S., Cakmak, R., Karam, G. (2006). GPS constraints on continental deformation in the Africa-Arabia-Eurasia continental collision zone and implications for the dynamics of plate interactions. *Journal of Geophysical Research: Solid Earth*, *111*(5), 1–26. https://doi.org/10.1029/2005JB004051

Schmittbuhl, J., Karabulut, H., Lengliné, O., & Bouchon, M. (2015). Seismicity distribution and locking depth along the MainMarmara Fault, Turkey. *Turkey, Geochem. Geophys. Geosyst., 17,954–965,* doi:10.1002/2015GC006120.

Schmittbuhl, J., Karabulut, H., Lengliné, O., & Bouchon, M. (2016). Long-lasting seismic repeaters in the Central Basin of the Main Marmara Fault. *Geophysical Research Letters 43*(18), 9527–9534. https://doi.org/10.1002/2016GL070505

Şengör, A. M. C., (1979). The North Anatolian transform fault: its age, offset and tectonic significance. *Journal of the Geological Society*, 136(3), 269-282. https://doi.org/10.1144/gsjgs.136.3.0269

Şengör, A. M. C., Grall, C., Imren, C., Le Pichon, X., Görür, N., Henry, P., Siyako, M. (2014). The geometry of the North Anatolian transform fault in the Sea of Marmara and
its temporal evolution: implications for the development of intracontinental transform faults1. *Canadian Journal of Earth Sciences*, *51*(3), 222–242. https://doi.org/10.1139/cjes-2013-0160

Snieder, R. (2002). Coda wave interferometry and the equilibration of energy in elastic media.
Physical Review E - Statistical Physics, Plasmas, Fluids, and Related Interdisciplinary
Topics, *66*(4), 8. https://doi.org/10.1103/PhysRevE.66.046615

Snieder, R., & Vrijlandt, M. (2005). Constraining the source separation with coda wave interferometry: Theory and application to earthquake doublets in the Hayward fault, California. *Journal of Geophysical Research: Solid Earth*, *110*(4), 1–15. https://doi.org/10.1029/2004JB003317

Tan, O., & Taymaz, T. (2006). Active tectonics of the Caucasus: Earthquake source mechanisms and rupture histories obtained from inversion of teleseismic body waveforms. *Special Paper of the Geological Society of America*, *409*(January 2006), 531–578. https://doi.org/10.1130/2006.2409(25)

Toda, S., Stein, R. S., Sevilgen, V., & Lin, J. (2011). Coulomb 3.3 Graphic-rich deformation & stress-change software for earthquake, tectonic and volcano research and teaching - User Guide. *USGS Open-File Report 2011-1060*, 63.

Wei, S., Zhan, Z., Tan, Y., Ni, S., & Helmberger, D. (2012). Locating earthquakes with surface waves and centroid moment tensor estimation. *Journal of Geophysical Research: Solid Earth*, *117*(4), 1–18. https://doi.org/10.1029/2011JB008501

Yang, H., L. Zhu, and R. Chu (2009). Fault-Plane Determination of the 18 April 2008 Mt. Carmel, Illinois, Earthquake by Detecting and Relocating Aftershocks, Bull. of Seismol. Soc. Am., 99(6), 3413-3420, doi: 10.1785/0120090038.

Yamamoto, R., Kido, M., Ohta, Y., Takahashi, N., Yamamoto, Y., Pinar, A., Kaneda, Y. (2019). Seafloor Geodesy Revealed Partial Creep of the North Anatolian Fault Submerged in the Sea of Marmara. *Geophysical Research Letters*, *46*(3), 1268–1275.

https://doi.org/10.1029/2018GL080984

Zhu, L., Helmberger, D. V., (1996). Advancement in Source Estimation Techniques Using Broadband Regional Seismograms. *Bulletin of the Seismological Society of America.* Vol. 86, No. 5, pp. 1634-1641

Zhu, L., Rivera, L. A. (2002). A note on the dynamic and static displacements from a point source in multilayered media. *Geophysical Journal International*, *148*(3), 619–627. https://doi.org/10.1046/j.1365-246X.2002.01610.x

Zhu, L., Ben-Zion, Y., (2013). Parametrization of general seismic potency and moment tensors for source inversion of seismic waveform data. *Geophysical Journal International.* Vol. 194, 2, pp. 839-843.

Zhu, L., X. F. Zhou, 2016, Seismic moment tensor inversion using 3D velocity model and its application to the 2013 Lushan earthquake sequence. *Physics and Chemistry of the Earth*, doi:10.1016/j.pce.2016.01.002-